
Article:
Wang, W. orcid.org/0000-0002-2294-7831, De Souza, M.M. orcid.org/0000-0002-7804-7154, Ghannam, R. et al. (2 more authors) (2023) A novel micro-scaled multi-layered optical stress sensor for force sensing. Journal of Computational Electronics, 22 (2). pp. 768-782. ISSN 1569-8025

https://doi.org/10.1007/s10825-023-02014-y

A Novel Micro-scaled Multi-layered Optical Stress Sensor for Force Sensing

Weijia Wang, Maria Merlyne De Souza, Rami Ghannam, Wen Jung Li, and Vellaisamy A. L. Roy

***Abstract*—Miniaturization and integration of sensors on chip has become essential with advancements of artificial intelligence (AI) and the Internet of Thing (IoT). The size of existing microbend optical stress sensors is too large for integration on a chip, necessisating fundamental change of structural design to achieve micron-sized lithography. In this regard, we demonstrate the design and analysis of a multi-layer- microbend optical stress sensor using an advanced Multiphysics simulation model that could be potentially embedded on chips after the experimental tests of the basic microbend optical stress sensor units. The sensor architecture is optimized not just in size but also the materials in the layers. A well optimized structure of Glass/Ag/SU8/PDMS architecture delivers best comprehensive performance resulting in a sensitivity in one pitch of 110.42 μm is 0.00935 N^{-1} with a linearity of R^2=0.99868 at a detectable range of 1200 N - 2800 N. This work paves way for embedding microbend optical stress sensors on chips to further accelerate sensors for communication and information technologies.**

***Index Terms*—Linearity, microbend optical stress sensor, micro-scaled, sensitivity, simulation**

I. Introduction

With the advent of artificial intelligence (AI) and Internet of Thing (IoT),[1-7] stress sensors have become increasingly important,[7-17] and require to be integrated[7, 18, 19] on-chip[7], for example, the micro-electromechanical systems (MEMS)-based 3D stress/strain sensor[22]. On the other hand, with advancements in robotic science, stress sensors are required in wearable devices and healthcare systems.[14, 23-28] An optical stress sensor[7] is based on detection of an optical signal rather than the resistance or capacitance in traditional stress sensors[7, 14, 32-39]. A microbend optical stress sensor utilises a toothlike microbend deformer for sensing.[7, 40] Since the materials of the microbend deformer and the optical fiber are non-ferromagnetic, with a low risk to electric sparking, they find suitability in extreme environments such as magnetic resonance imaging (MRI) and explosives respectively.[7, 41-44] In addition, due to advantages of flexibility, sensitivity, reliability, and low cost, microbend optical stress sensors can be used to detect pressure in 2D fiber arrays[29], as anti-squeeze detectors of car windows[21], detection of respiration and heartbeat[31, 45], hydrophones, chemical sensing, etc.[7, 46, 47] However, the size of existing microbend optical stress sensors (see Table I) is in the millimeter (mm) or centimeter (cm) scale.[7] The size of the optical fiber is a limitation for the miniaturization of the microbend optical stress sensor, and it is too large for integration on a chip.

In order to realize the miniaturization, a fundamental change to the structural design becomes necessary. Therefore, in this work, a multi-layer- microbend optical stress sensor was designed and analyzed using a Finite Element Method (FEM) simulation tool and benchmarked using an experiment verified model, to arrive at figures for the sensitivity and linearity of the model. On-chip Scaling was achieved using SU8 and Ag film to create multilayered fiber structures. A well optimized structure of Glass/Ag/SU8/PDMS architecture delivers best comprehensive performance in terms of sensitivity, linearity, and detectable range examined in this work, and it shows potential to be fabricated on chip. The materials with appropriate properties and parameters were selected, and the simulation results in this work were predictable and reasonable. In addition, the simulation results in this work were predicted and validated by the properties tests of the microbend optical stress sensor units with the standard graded index multimode fiber (GI MMF) and microbend deformers, and also validated by the existing simulation and experimental results of microbend sensors in the literature, which shown the design and performance of our device models were feasible and reliable. This work will promote the miniaturization and integration of

TABLE I
SOME EXAMPLES OF THE SIZE SCALE OF CURRENT MICROBEND OPTICAL STRESS SENSORS

Sensors	Size scale	Ref.
Embedded fibre optic microbend sensor	mm	[20]
Plastic optical fiber microbend anti-squeeze sensor	mm	[21]
Fiber optic microbend tactile sensor array	mm	[29]
Fiber optic microbend sensor	cm	[30]
Textile fiber optic microbend sensor	cm	[31]

The authors acknowledge the grant from the Research Grant Council of HKSAR (Grant No. CityU 11210819). *(Corresponding author: Vellaisamy A. L. Roy.)*

W. Wang is with the State Key Laboratory for Millimeter and Terahertz Waves and Department of Materials Science and Engineering, City University of Hong Kong, Tat Chee Avenue, Kowloon, Hong Kong SAR, China. (e-mail: weijwang4-c@my.cityu.edu.hk).

M. M. De Souza is with the Department of Electronic and Electrical Engineering, University of Sheffield, Sheffield, S3 7HQ, United Kingdom. (e-mail: m.desouza@sheffield.ac.uk).

R. Ghannam and V. A. L. Roy are with the James Watt School of Engineering, University of Glasgow, G12 8QQ, United Kingdom. (e-mail: rami.ghannam@glasgow.ac.uk; Roy.Vellaisamy@glasgow.ac.uk).

W. J. Li is with the Department of Mechanical Engineering, City University of Hong Kong, Tat Chee Avenue, Kowloon, Hong Kong SAR, China. (e-mail: wenjli@cityu.edu.hk).

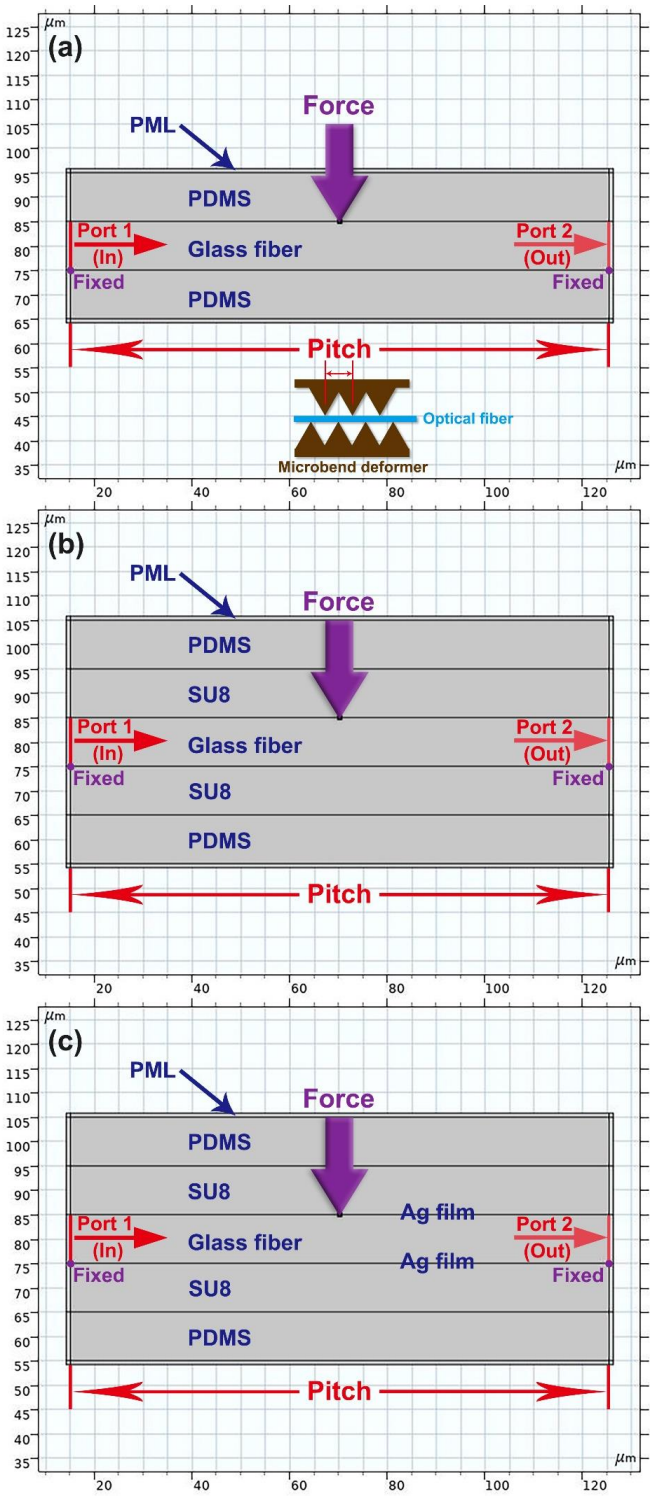

Fig. 1. The structure and simulation conditions of the sensor models in this work: (a) the Glass/PDMS model, (b) the Glass/SU8/PDMS model, and (c) the Glass/Ag/SU8/PDMS model.

microbend optical stress sensors and embed them on chips, which will make them have wider application fields in future.

II. Methodology

A. Simulation part

1) Simulation software

The simulations in this work were conducted using the COMSOL Multiphysics® software with the solid mechanics interface and the electromagnetic waves, frequency domain interface.[48] In the solid mechanics simulation, stress and strain follow Hooke's law:[49, 50]

$$\sigma_m = E_m \varepsilon_m \quad (1)$$

where σ_m and ε_m are the stress and strain of the models, respectively. E_m is Young's modulus of the materials.

The relationship between strain and displacement is:[51]

$$\boldsymbol{\varepsilon} = \frac{\nabla \boldsymbol{u} + (\nabla \boldsymbol{u})^T}{2} \quad (2)$$

where $\boldsymbol{\varepsilon}$ is the infinitesimal strain tensor, and $\boldsymbol{u}$ is the displacement variables.

The von Mises stress which describes the maximum distortion energy of the model under load is used to present the simulation results of the solid mechanics:[52]

$$\sigma_{VM} = \frac{1}{\sqrt{2}}\sqrt{(\sigma_1 - \sigma_2)^2 + (\sigma_2 - \sigma_3)^2 + (\sigma_3 - \sigma_1)^2} \quad (3)$$

where σ_{VM} is von Mises stress, and σ_1, σ_2, and σ_3 are the principal stresses.

In the electromagnetic domain simulation, the wave equation is:[53]

$$\nabla \times (\nabla \times \boldsymbol{E}) - k_0^2 n^2 \boldsymbol{E} = 0 \quad (4)$$

where $\boldsymbol{E}$ is the distribution of the electric field of the light, k_0 is wave number in free space, n is the refractive index.

2) Geometric modeling

A conventional structure [Fig. 1(a)] and two proposed structures [Fig. 1(b) and 1(c)] will be studied in this work. The proposed structures were developed based on the conventional structure to improve its performance. The conventional structure is shown in Fig. 1(a) (The inset of Fig. 1(a) shows a simple schematic diagram of the structure of the microbend optical stress sensor), which is the longitudinal section of a fiber with different layers along the long axis of the center. A force is applied to bend the entire structure to obtain the changes on the light intensity. The core layer is glass,[54-56] coated with a polydimethylsiloxane (PDMS) layer (Glass/PDMS model). The diameter of the core layer and the thickness of the PDMS layer are both 10 μm. It is realizable to build the PDMS patterns at the dimension less than 10 μm in the literature.[57] There are two ports (port 1 and port 2) set at the two ends of the core layer for light in and out, respectively.

The sensitivity of the microbend optical stress sensor is related to the distance between the two adjacent teeth on one side of the microbend deformer which is called the pitch.[7, 40, 58] The pitch is calculated as follows:[7, 58, 59]

$$\text{Pitch} = \frac{2\pi R n_1}{\text{N.A.}} \quad (5)$$

where R is the radius of the core layer in the optical fiber, n_1 is the refractive index of the core layer, N.A. is the numerical aperture of the optical fiber estimated as:[60-62]

$$\text{N.A.} = \sqrt{n_1^2 - n_2^2} \quad (6)$$

where n_2 is the refractive index of the cladding layer. Thus, a suitable pitch can be calculated as:

$$\text{Pitch} = \frac{2\pi R n_1}{\sqrt{n_1^2 - n_2^2}} \quad (7)$$

The two proposed structures are Glass/SU8/PDMS model [Fig. 1(b)] and Glass/Ag/SU8/PDMS model [Fig. 1(c)]. For the Glass/SU8/PDMS model, the SU8 layer is added as a coating layer between the glass fiber core and the PDMS layer based on the Glass/PDMS model, and its thickness is also 10 μm. The SU8 patterns can be built at the dimension about 10 μm or less

in the literature.[63, 64] For convenience of comparison, the pitch of the Glass/PDMS model continues to be used in the Glass/SU8/PDMS model. The structure of the Glass/Ag/SU8/PDMS model is similar as the Glass/SU8/PDMS model except the 10 nm-thickness Ag film is added at the upper and lower boundaries between the glass fiber core and the SU8 layer and simulated by transition boundary condition (TBC) [Fig. 1(c)]. Other simulation conditions are same as the ones of the Glass/SU8/PDMS model [Fig. 1(b)].

3) Materials properties setup

The refractive index of the core layer and the PDMS cladding layer are respectively set as n_{glass}=1.476 and n_{PDMS}=1.415.[65, 66] Therefore, the calculated pitch is 110.42 μm. The thin layer around the entire model is called the perfectly matched layer (PML), which is used to absorb the emergent light and simulate the infinite outside space. Other material parameters from built-in data from COMSOL Multiphysics® software are highlighted in Table II.

4) Physical fields setup

a) Solid mechanics interface

The left-bottom and right-bottom points of the core layer are fixed by the pitch. Force is applied at the midpoint of the upper border of the core layer in a downward direction along the y-axis, as shown in Fig. 1. This simulates the deformation over one pitch of the optical fiber under pressure between the toothlike microbend deformers.

TABLE II
OTHER MAIN PROPERTIES OF THE MATERIALS IN THIS WORK (T=293.15 K)

Materials	Density (kg/m^3)	Young's modulus (Pa)	Poisson's ratio
Glass	2203	7.31×10^{10}	0.17
PDMS	970	7.50×10^{5}	0.49
SU8	1392.771-0.6426783T+1.575939 $\times10^{-4}$T^2	8.986054×10^{9}-2.738131$\times$ 10^{7}T+26053.55T^2	0.33

b) Electromagnetic waves, frequency domain interface

The wave excitation of port 1 is turned on, and the incident light set as λ=633 nm, with a power of 1 W enters into the fiber from port 1. The wave excitation of port 2 is turned off. The electric field of the incident light is set as:

$$\mathbf{E} = \begin{bmatrix} 0 \\ 0 \\ 1 \end{bmatrix} \text{V/m} \tag{8}$$

The propagation constant of each port is set as:[62, 67]

$$\beta = \frac{2\pi n_{\text{glass}}}{\lambda} \tag{9}$$

The thickness of the PML is set as 10 mesh layers of the electromagnetic waves, frequency domain interface to absorb the emergent light.[68-71]

5) Results

The normalized output power is calculated as:

$$P_{\text{out}}\,(\%) = \frac{P_2}{|P_1|} \times 100\% \tag{10}$$

where P_1 and P_2 are the line integration values of power outflow, time average of port 1 and port 2, respectively. Since the value of P_1 is negative, the absolute value of P_1 is used.

B. Experimental part

The experimental platform used for the properties tests of the microbend optical stress sensor units in this work is shown in Fig. 2. The microbend deformers used in this work are fabricated by Al-7075 alloy which are shown in the inset of Fig. 2. The pitches of the microbend deformers are 3.0 mm, 1.5 mm, and 1.0 mm. The 633 nm laser (THORLABS, 10 mW) was focused on one end of the standard GI MMF. The optical fiber was fixed so that it can traverse the microbend deformer between its two layers of the toothlike structure, and the light power was measured by a light power meter (Newport, 843-R) on the other end of GI MMF. The microbend deformer was fixed on the probe of the force detector (Force Gauge Model M5-5). When the probe of the force detector moves down, the GI MMF will be pressed by the microbend deformer, and then the force values can be read. For the repeatability tests, the cyclic force was applied to the microbend deformers, and the light power and the force values were measured.

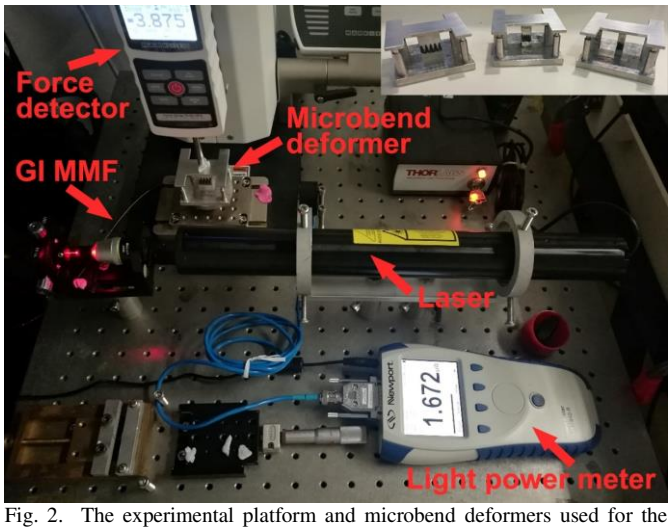

Fig. 2. The experimental platform and microbend deformers used for the properties tests of the microbend optical stress sensor units in this work.

III. Results and Discussion

A. *Properties tests of microbend optical stress sensor units*

The optical-force properties of the microbend optical stress sensor units with various pitches of microbend deformers are shown in Fig. 3(a). All the microbend optical stress sensor units in this work have the expected performance. The emergent light power decreases when the force increases, and it decreases to near 0 μW when the force is large enough. The sensor unit with 1.5 mm-pitch microbend deformer has the largest detectable range of force which can reach 13 N before broken. With the increasing of the pitch of the microbend deformer, the anti-pressure performance will be better, for example, the sensor unit with 1.0-mm pitch microbend deformer had the higher slop of power/force, which suggests that it is more sensitive.

To investigate the stabilization and the repeatability of the microbend optical stress sensor units, the cyclic force was applied to the sensor systems. The cyclic optical-force responds of the microbend optical stress sensor units with the microbend deformer pitches of 3.0 mm, 1.5 mm, and 1.0 mm are shown in Fig. 3(b), (c), and (d), respectively. After applying the force for one period, the output power of all the samples can recover upto near the initial state, which suggests that the sensors can be self-recovered and ready for the new round test. Therefore, their repeatability of the mechanical and optical properties are satisfactory, and the sensor system is stable and reliable.

Through the experiments and analysis of the properties test of the microbend optical stress sensor units with various pitches of microbend deformers, the simulation results in our work can be predicted. Indeed, after the simulation, the decreasing variation tendency of the normalized output power of our simulation models is similar as the results of the experiments in this work, which suggests that our simulation is valid and reliable. Our simulation results have also been validated by the existing simulation and experimental results of microbend sensors in the literature. The power loss due to the microbend in the fiber core in our results is also shown in the simulation results in the literature.[72] In addition, the variation tendency of the normalized output power in our simulation results of the Glass/PDMS model is similar as the experiment and simulation results in the literatures, which also suggests that our simulation method is valid and reliable.[40, 58, 73] For the simplification of the models and emphasizing the effect of the deformation due to the applied force to the normalized output power, the changes of refractive index due to stress-optic effect were not included in this work.[53, 73]

B. *The Glass/PDMS model – Conventional model*

The applied force range of the Glass/PDMS model is 0-2200 N. The stress distribution of Glass/PDMS model at 2200 N is shown in Fig. 4(a). The stress is mainly distributed on the glass fiber around the point of applied force and its opposite side, and around the fixed points. The relationship between the normalized output power and applied force of Glass/PDMS model is shown in Fig. 4(d). With an increase of the applied force, from 0 N to 1200 N, the normalized output power has no obvious reduction. From 1200 N to 1600 N, the normalized output power decreases from 96.75% to 58.14% with an increase of the applied force. From 1600 N to 2200 N, the decreasing tendency of normalized output power becomes flat.

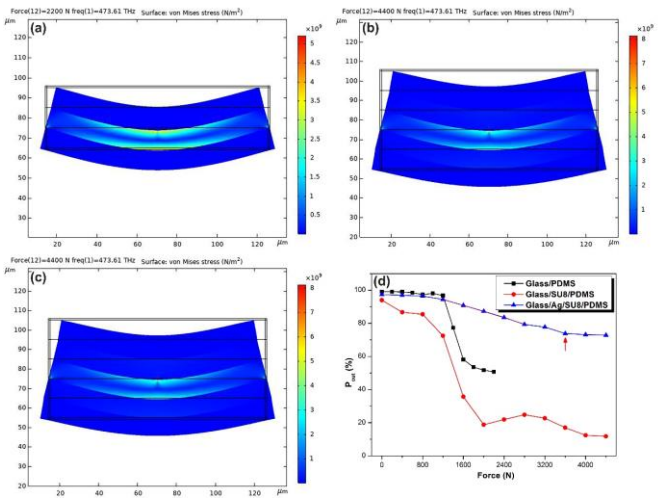

Fig. 4. The stress distribution and the relationship between the normalized output power and applied force of the sensor models in this work: (a) the stress distribution of the Glass/PDMS model, (b) the stress distribution of the Glass/SU8/PDMS model, (c) the stress distribution of the Glass/Ag/SU8/PDMS model, and (d) the relationship between the normalized output power and applied force of the sensor models in this work.

The light power distributions of Glass/PDMS model at 0 N, 800 N, 1400 N and 2200 N are shown in Fig. 5. The refractive index of glass is higher than that of PDMS. Thus, when the light propagates from glass to the PDMS layer, the total reflection will occur when the incident angle is larger than the critical angle. Increasing the applied force results in bending of the tooth comb. When the force is below 1200 N, the bending degree is low. Thus, the incident angle of light at the interface between the glass fiber core to the PDMS layer can be large enough for the total reflection at this stage, and mainly due to total internal reflection, the loss of light in the glass fiber core is low, and there is no obvious reduction of normalized output power in the applied force range from 0 N to 1200 N (e.g. 0 N and 800 N in Fig. 5). When the force is higher than 1200 N, refracted light from the glass fiber core to the PDMS layer begins to appear. Thus, the normalized output power decreases obviously, which agrees with the principle of power loss (e.g. 1400 N in Fig. 5).[7, 74-76] Due to the width of the incident light beam, and the arcuate bending structure of the interface

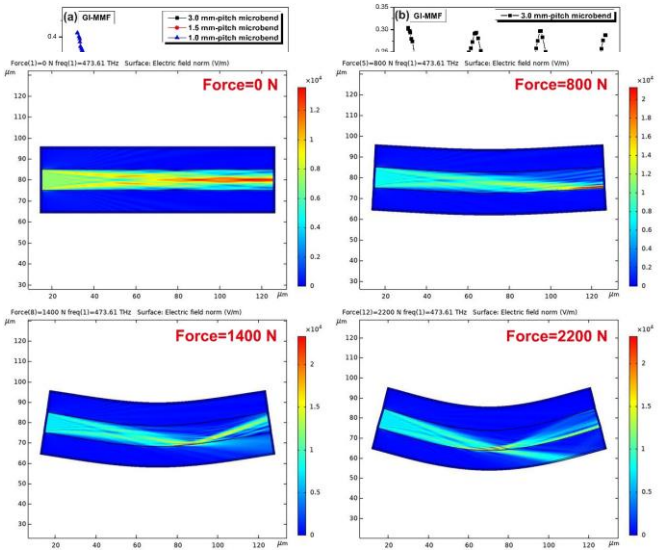

Fig. 5. The light power distributions of Glass/PDMS model.

between the glass fiber core and PDMS layer, some fraction of the reflected light still follows total internal reflection. In addition, the relationship between the reflectivity and the incident angle will also affect the normalized output power. This explains the decreasing tendency of normalized output power to become flat from 1600 N to 2200 N (e.g. 2200 N in Fig. 5).

In summary, the normalized output power in the Glass/PDMS model responds to the applied force. Because of the total internal reflection, however, the normalized output power has no obvious changes at a large force range (0-1200 N), which results in the small detectable range and low sensitivity. Therefore, a type of material with the refractive index higher than glass is needed to weaken the total internal reflection and improve the sensitivity of the model.

C. Glass/SU8/PDMS model – improving the sensitivity

SU8 is a type of UV photoresist that has wide application in MEMS, waveguides, superhydrophobic surface, etc.[63, 64, 77-82] Also, it has relatively high refractive index n_{SU8}=1.5912.[83] Thus, SU8 was selected to coat outside the glass fiber core of the Glass/PDMS model to weaken the total internal reflection in the proposed Glass/SU8/PDMS model [Fig. 1(b)]. Since the whole model is thicker, in order to keep a similar bending level as the Glass/PDMS model, the applied force range in Glass/SU8/PDMS model is extended to 0-4400 N. Other structures and simulation conditions in the Glass/SU8/PDMS model remain the same.

The stress distribution of Glass/SU8/PDMS model at 4400 N is shown in Fig. 4(b). Similar as it was in Glass/PDMS model, the stress is also mainly distributed on the glass fiber around the point of applied force and its opposite side, and around the fixed points. The relationship between the normalized output power and applied force of Glass/SU8/PDMS model is shown in Fig. 4(d). With the increasing of the applied force, from 0 N to 2000 N, the normalized output power decreasing from 93.99% to 18.79%. From 2000 N to 4400 N, the normalized output power increases slightly first and then decreases again. The light power distributions of Glass/SU8/PDMS model at 0 N, 1600 N, 2800 N and 4400 N are shown in Fig. 6. Due to the refractive index of glass is lower than the one of SU8, the total reflection effect at the interface from glass to SU8 does not exist. Thus, when the whole fiber start bending, even though the bending is in a relatively low degree, the light in the glass fiber core can transmit to SU8 layer in a relatively high power, which causes the power loss of light in glass core, and results in the decreasing of the normalized output power in the applied force range from 0 N to 2000 N. (e.g. 0 N and 1600 N in Fig. 6). With the increasing of the applied force, the bending degree increases. Due to the refractive index of SU8 is higher than the one of PDMS, the total reflection effect at the interface from SU8 to PDMS will make the light in the SU8 layer reflect back to the glass fiber core, which makes the slight increasing of the normalized output power from 2000 N to 2800 N (e.g. 2800 N in Fig. 6). When the applied force continues increasing, the bending level also continues increasing, and the light power reflected back from the cladding layers becomes lower. Thus, the normalized output power decreases again from 2800 N to 4400 N (e.g. 4400 N in Fig. 6).

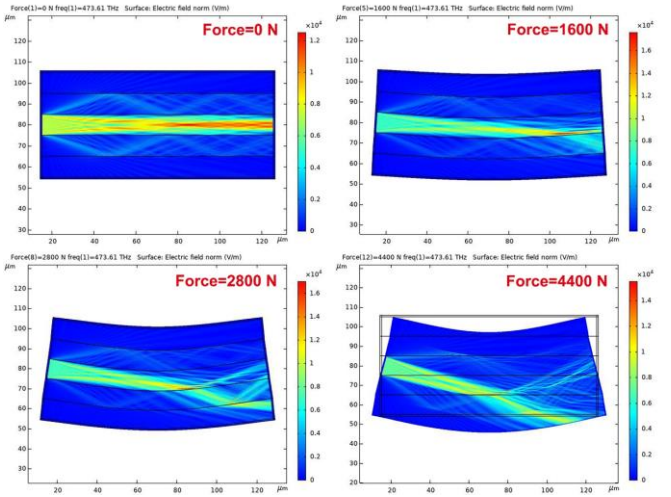

Fig. 6. The light power distributions of Glass/SU8/PDMS model.

In summary, the responding range of the normalized output power is larger when the SU8 layer is added. However, due to the weak limitation of the light transmitted out from and reflected back to the glass fiber core, the linearity between the normalized output power and the applied force is poor. Therefore, one type of material which can mitigate the transmission of light at the interface between glass fiber core and SU8 layer is needed to further improve the linearity of the model.

D. Glass/Ag/SU8/PDMS model – for improved linearity

A beam splitter is a component which can separate one light beam into two parts: the reflected and the transmitted.[84, 85] It has wide application in Michelson-type spectrometers and solar cell.[86, 87] In addition, a Ag film can be used in the beam splitter between, for example, two tin-doped indium oxide (ITO) films or two glass layers.[84, 86] If the Ag film is sufficiently thick, it could act like a mirror to reflect the light. If the power of the reflected and the transmitted light separated by the beam splitter at a certain incident angle are adjusted by changing the thickness of the Ag film, then the Ag film can be introduced into our model to adjust the transmission of light at the interface between the glass fiber core and SU8 layer.[86] Therefore, referenced the "beam_splitter" case in the application libraries of the COMSOL Multiphysics® software and under the inspiration of the beam splitter, the reflectivity of different thickness of Ag film and incident angles in beam splitter was investigated, and the Ag film was introduced into the Glass/SU8/PDMS model to build the Glass/Ag/SU8/PDMS model.[48, 84-87]

The model for the investigation of the reflectivity of different thickness of Ag film and incident angles from glass layer to SU8 layer is shown in Fig. 7(a), which referenced the "beam_splitter" case in the application libraries of the COMSOL Multiphysics® software.[48] The entire model was built based on a circle with the radius of 25 μm, divided into two parts by an upper right-left bottom diameter line. The material of upper left part is glass, and the one of bottom right part is SU8. The width of the port is 10 μm. The scattering boundary condition (SBC) was used at the circle boundary except the port to absorb the emergent light and simulate the infinite outside space only in this model [Fig. 7(a)]. The main simulation parameters of the port and light in this model is

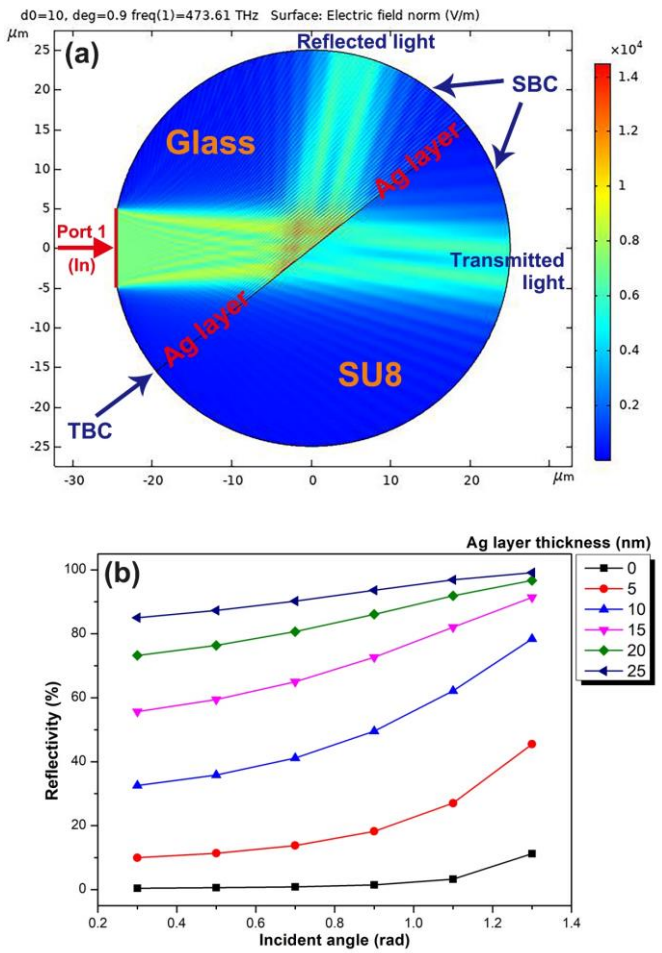

Fig. 7. The model for the investigation of the reflectivity of different thickness of Ag film and incident angles from glass layer to SU8 layer (a), and the reflectivity of the Ag film under different incident angles and Ag film thickness from glass layer to SU8 layer (b).

similar as the ones of other models in this work. The Ag layer is set on the diameter line, and it can rotate around the center of the circle to change the incident angle, and the range of incident angle is 0.3-1.3 rad. The Ag layer is simulated by TBC, its relative permittivity, relative permeability, and electrical conductivity are set as ε_r=-16.72+1.66i,[88] μ_r=1, and σ=0 S/m, respectively. The thickness range of Ag film is 0-25 nm. The reflectivity of the Ag film can be calculated as:

$$\text{Reflectivity (\%)} = \frac{P_R}{|P_1|} \times 100\% \qquad (11)$$

where P_R is the power of reflected light which refers to line integration value of power outflow, time average of the upper arc between the top point of port 1 and the upper right point of the diameter line in Fig. 7(a). P_1 here is the line integration value of power outflow, time average of port 1 in Fig. 7(a).

The reflectivity of the Ag film under different incident angles and Ag film thickness from glass layer to SU8 layer is shown in Fig. 7(b). With the increasing of the incident angle, the reflectivity of the Ag film of each Ag film thickness is increasing. For a certain incident angle, with the increasing of the thickness of Ag film, the reflectivity is also increasing. For a 10 nm thickness of Ag film, the increasing tendency of reflectivity is relatively near the linear tendency, and at the same time, the increasing range of reflectivity from 0.3 rad to 1.3 rad is the largest, which improves the linearity and sensitivity of the model, respectively. Therefore, the 10 nm-thickness Ag film was selected to be added into the Glass/SU8/PDMS model. A benefit of the Ag film between the glass fiber core and the coating layer in the fiber, is that it reduces the likelihood of sparks when light propagates in the fiber. Also, Ag almost has no magnetic activities under the external magnetic fields confirming its suitability in extreme environments such as the explosive or the MRI environment, respectively.

The stress distribution of Glass/Ag/SU8/PDMS model at 4400 N is shown in Fig. 4(c), which is similar as it was in the Glass/SU8/PDMS model. The relationship between the normalized output power and applied force of Glass/Ag/SU8/PDMS model is shown in Fig. 4(d). With the increasing of the applied force, the normalized output power decreases monotonically. From 1200 N to 2800 N, the linearity

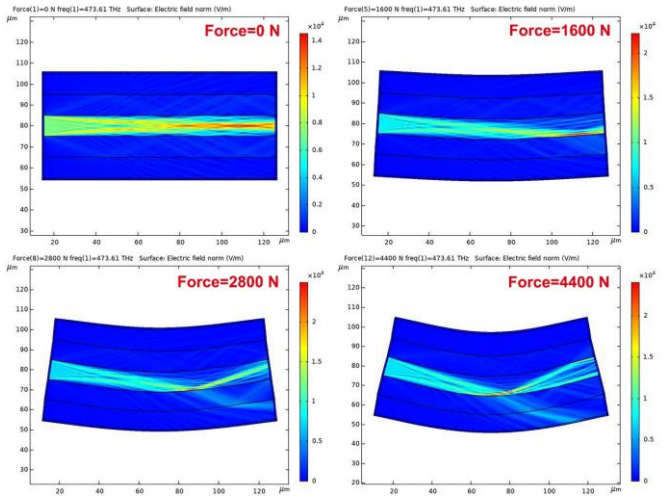

Fig. 8. The light power distributions of Glass/Ag/SU8/PDMS model.

between the normalized output power and the applied force is good, the equation is y=-0.00935x+105.76475, and the R^2=0.99868. Thus, its sensitivity from 1200 N to 2800 N can be 0.00935 N^{-1}. The detectable range is larger, although its sensitivity is relatively lower than the other two models in this work. From 0 N to 1200 N and from 2800 N to 4400 N, the decreasing rate of normalized output power is almost slight. The light power distributions of Glass/Ag/SU8/PDMS model at 0 N, 1600 N, 2800 N and 4400 N are shown in Fig. 8. With an increase of the applied force, the entire structure bends, but the light power transmitted from the glass fiber core to the SU8 layer is much lower than that in the Glass/SU8/PDMS model, which benefits from the mitigation effect for the transmission of light of the Ag film at the interface between the glass fiber core and SU8 layer, and it makes the light power lost slowly. At the same time, the Ag film also reduces the light power reflected back from the SU8 layer to the glass fiber core (e.g. 4400 N in Fig. 8). When the applied force is in the large range [e.g. the red arrow position in Fig. 4(d)], due to the bending of the entire structure, some parts of the light in the glass fiber core will transmit into the cladding layer through the upper boundary, which may result in a relatively high loss of the normalized output power. However, it is not in the linearity range of detection, and may make little effect for sensing. Therefore, the adding of the Ag film can improve the linearity

and detectable range effectively, and the comprehensive performance of the Glass/Ag/SU8/PDMS is better than the Glass/PDMS model and the Glass/SU8/PDMS model although there is a decreasing of its sensitivity.

IV. Conclusions

In this work, the design and performance of a novel micro-scaled microbend optical stress sensor is modeled and simulated after the experimental tests of the basic microbend optical stress sensor units. To improve the comprehensive performance of the micro-scaled sensor, the SU8 layer and Ag film are introduced into the initial Glass/PDMS core-cladding design successively to develop proposed Glass/SU8/PDMS and Glass/Ag/SU8/PDMS multi-layered architectures, respectively. It is found that the Glass/Ag/SU8/PDMS architecture shows good comprehensive performance among the three designs in this work in a working range from 1200 N to 2800 N. This work will promote the development of the microbend optical stress sensor on the micro-scaled and miniaturization direction, and extend the application fields in the future.

References

[1] S. Kalasin, P. Sangnuang, and W. Surareungchai, "Satellite-Based Sensor for Environmental Heat-Stress Sweat Creatinine Monitoring: The Remote Artificial Intelligence-Assisted Epidermal Wearable Sensing for Health Evaluation," *ACS Biomater. Sci. Eng.,* vol. 7, no. 1, pp. 322-334, 2021/01/11 2021

[2] H. Goyal *et al.*, "Application of artificial intelligence in pancreaticobiliary diseases," *Ther. Adv. Gastrointest. Endosc.,* vol. 14, Feb 2021

[3] H. Q. Wu and Q. H. Dai, "Artificial intelligence accelerated by light," *Nature,* vol. 589, no. 7840, pp. 25-26, Jan 2021

[4] T. Jacques *et al.*, "Proposals for the use of artificial intelligence in emergency radiology," *Diagn. Interv. Imaging,* vol. 102, no. 2, pp. 63-68, 2021/02/01/ 2021

[5] X. Li, "Research on tourism industrial cluster and information platform based on Internet of things technology," *Int. J. Distrib. Sens. N.,* vol. 15, no. 7, p. DOI: 10.1177/1550147719858840, Jul 2019

[6] K. L. M. Ang and J. K. P. Seng, "Application Specific Internet of Things (ASIoTs): Taxonomy, applications, use case and future directions," *IEEE Access,* vol. 7, pp. 56577-56590, 2019

[7] W. Wang, H. H. P. Yiu, W. J. Li, and V. A. L. Roy, "The Principle and Architectures of Optical Stress Sensors and the Progress on the Development of Microbend Optical Sensors," *Adv. Opt. Mater.,* vol. 9, no. 10, p. 2001693, 2021

[8] J. Ge *et al.*, "A stretchable electronic fabric artificial skin with pressure-, lateral strain-, and flexion-sensitive properties," *Adv. Mater.,* vol. 28, no. 4, pp. 722-728, Jan 27 2016

[9] F. Hu, L. Zhang, W. Z. Liu, X. X. Guo, L. Shi, and X. Y. Liu, "Gel-based artificial photonic skin to sense a gentle touch by reflection," *ACS Appl. Mater. Interfaces,* vol. 11, no. 17, pp. 15195-15200, May 2019

[10] S. H. Heo, C. Kim, T. S. Kim, and H. S. Park, "Human-palm-inspired artificial skin material enhances operational functionality of hand manipulation," *Adv. Funct. Mater.,* vol. 30, p. 2002360, 2020

[11] F. Liang *et al.*, "Layer-by-layer assembly of nanofiber/nanoparticle artificial skin for strain-insensitive UV shielding and visualized UV detection," *Adv. Mater. Technol.,* vol. 5, no. 4, p. 1900976, Apr 2020

[12] S. Park, B. G. Shin, S. Jang, and K. Chung, "Three-Dimensional Self-Healable Touch Sensing Artificial Skin Device," *ACS Appl. Mater. Interfaces,* vol. 12, no. 3, pp. 3953-3960, Jan 2020

[13] Z. W. K. Low *et al.*, "Using artificial skin devices as skin replacements: Insights into superficial treatment," *Small,* vol. 15, no. 9, p. 1805453, Mar 2019

[14] Q. J. Sun *et al.*, "Highly sensitive and ultrastable skin sensors for biopressure and bioforce measurements based on hierarchical microstructures," *ACS Appl. Mater. Interfaces,* vol. 10, no. 4, pp. 4086-4094, Jan 2018

[15] Q.-J. Sun *et al.*, "Bioinspired, Self-Powered, and Highly Sensitive Electronic Skin for Sensing Static and Dynamic Pressures," *ACS Appl. Mater. Interfaces,* vol. 12, no. 33, pp. 37239-37247, 2020/08/19 2020

[16] Q.-J. Sun *et al.*, "Fingertip-Skin-Inspired Highly Sensitive and Multifunctional Sensor with Hierarchically Structured Conductive Graphite/Polydimethylsiloxane Foams," *Adv. Funct. Mater.,* vol. 29, no. 18, p. 1808829, 2019

[17] Q.-J. Sun *et al.*, "Printed High-k Dielectric for Flexible Low-Power Extended Gate Field-Effect Transistor in Sensing Pressure," *ACS Appl. Electron. Mater.,* vol. 1, no. 5, pp. 711-717, 2019/05/28 2019

[18] Y. Lim and J. Park, "Sensor resource sharing approaches in sensor-cloud infrastructure," *Int. J. Distrib. Sens. N.,* vol. 2014, p. 476090, 2014

[19] N. C. Basjaruddin, F. Syahbarudin, and E. Sutjiredjeki, "Measurement Device for Stress Level and Vital Sign Based on Sensor Fusion," *Healthc. Inform. Res.,* vol. 27, no. 1, pp. 11-18, Jan 2021

[20] N. K. Pandey and B. C. Yadav, "Embedded fibre optic microbend sensor for measurement of high pressure and crack detection," *Sens. Actuator A-Phys.,* vol. 128, no. 1, pp. 33-36, Mar 2006

[21] M. Linec and D. Donlagic, "A plastic optical fiber microbend sensor used as a low-cost anti-squeeze detector," *IEEE Sens. J.,* vol. 7, no. 9-10, pp. 1262-1267, Sep-Oct 2007

[22] M. O. Kayed, A. A. Balbola, E. Lou, and W. A. Moussa, "Development of MEMS-based piezoresistive 3D stress/strain sensor using strain technology and smart temperature compensation," *J. Micromech. Microeng.,* vol. 31, no. 3, p. 035010, 2021/02/08 2021

[23] T. Tran Quang and N.-E. Lee, "Flexible and stretchable physical sensor integrated platforms for wearable human-activity monitoring and personal healthcare," *Adv. Mater.,* vol. 28, no. 22, pp. 4338-4372, Jun 8 2016

[24] Y. Khan, A. E. Ostfeld, C. M. Lochner, A. Pierre, and A. C. Arias, "Monitoring of vital signs with flexible and wearable medical devices," *Adv. Mater.,* vol. 28, no. 22, pp. 4373-4395, Jun 8 2016

[25] C. Pang *et al.*, "Highly skin-conformal microhairy sensor for pulse signal amplification," *Adv. Mater.,* vol. 27, no. 4, pp. 634-640, Jan 27 2015

[26] S. Milici, A. Lazaro, R. Villarino, D. Girbau, and M. Magnarosa, "Wireless Wearable Magnetometer-Based Sensor for Sleep Quality Monitoring," *IEEE Sens. J.,* vol. 18, no. 5, pp. 2145-2152, Mar 1 2018

[27] J. Chen, M. Abbod, and J. S. Shieh, "Pain and Stress Detection Using Wearable Sensors and Devices-A Review," *Sensors,* vol. 21, no. 4, p. 1030, Feb 2021

[28] A. Georgopoulou, S. Michel, B. Vanderborght, and F. Clemens, "Piezoresistive sensor fiber composites based on silicone elastomers for the monitoring of the position of a robot arm," *Sens. Actuator. A Phys.,* vol. 318, p. 112433, 2021/02/01/ 2021

[29] D. T. Jenstrom and C. L. Chen, "A fiber optic microbend tactile sensor array," *Sens. Actuators,* vol. 20, no. 3, pp. 239-248, Dec 1989

[30] F. Luo, J. Y. Liu, N. B. Ma, and T. F. Morse, "A fiber optic microbend sensor for distributed sensing application in the structural strain monitoring," *Sens. Actuator A-Phys.,* vol. 75, no. 1, pp. 41-44, May 1999

[31] X. F. Yang *et al.*, "Textile fiber optic microbend sensor used for heartbeat and respiration monitoring," *IEEE Sens. J.,* vol. 15, no. 2, pp. 757-761, Feb 2015

[32] X. Wang, Z. Liu, and T. Zhang, "Flexible sensing electronics for wearable/attachable health monitoring," *Small,* vol. 13, no. 25, p. 1602790, Jul 5 2017

[33] Kenry, J. C. Yeo, and C. T. Lim, "Emerging flexible and wearable physical sensing platforms for healthcare and biomedical applications," *Microsyst. Nanoeng.,* vol. 2, p. 16043, Sep 2016

[34] J. L. Wang, C. H. Lu, and K. Zhang, "Textile-Based Strain Sensor for Human Motion Detection," *Energy Environ. Mater.,* vol. 3, no. 1, pp. 80-100, Mar 2020

[35] W. Chen and X. Yan, "Progress in achieving high-performance piezoresistive and capacitive flexible pressure sensors: A review," *J. Mater. Sci. Technol.,* vol. 43, pp. 175-188, 2020/04/15/ 2020

[36] A. Rivadeneyra and J. A. Lopez-Villanueva, "Recent Advances in Printed Capacitive Sensors," *Micromachines,* vol. 11, no. 4, p. 20, Apr 2020

[37] P. S. Song *et al.*, "Recent Progress of Miniature MEMS Pressure Sensors," *Micromachines,* vol. 11, no. 1, p. 38, Jan 2020

[38] T. W. Lu and P. T. Lee, "Ultra-high sensitivity optical stress sensor based on double-layered photonic crystal microcavity," *Opt. Express,* vol. 17, no. 3, pp. 1518-1526, Feb 2009

[39] R. Gafsi, P. Lecoy, and A. Malki, "Stress optical fiber sensor using light coupling between two laterally fused multimode optical fibers," *Appl. Optics,* vol. 37, no. 16, pp. 3417-3425, Jun 1998

[40] L. Su, K. S. Chiang, and C. Lu, "Fiber Bragg-grating incorporated microbend sensor for simultaneous mechanical parameter and temperature

measurement," *IEEE Photonics Technol. Lett.,* vol. 17, no. 12, pp. 2697-2699, Dec 2005

[41] Z. H. Chen, D. Lau, J. T. Teo, S. H. Ng, X. F. Yang, and P. L. Kei, "Simultaneous measurement of breathing rate and heart rate using a microbend multimode fiber optic sensor," *J. Biomed. Opt.,* vol. 19, no. 5, p. 057001, May 2014

[42] A. Bichler, S. Lecler, B. Serio, S. Fischer, and P. Pfeiffer, "Mode couplings and elasto-optic effects study in a proposed mechanical microperturbed multimode optical fiber sensor," *J. Opt. Soc. Am. A-Opt. Image Sci. Vis.,* vol. 29, no. 11, pp. 2386-2393, Nov 2012

[43] A. MacLean, C. Moran, W. Johnstone, B. Culshaw, D. Marsh, and P. Parker, "Detection of hydrocarbon fuel spills using a distributed fibre optic sensor," *Sens. Actuator A-Phys.,* vol. 109, no. 1-2, pp. 60-67, Dec 2003

[44] D. Lau *et al.*, "Intensity-modulated microbend fiber optic sensor for respiratory monitoring and gating during MRI," *IEEE Trans. Biomed. Eng.,* vol. 60, no. 9, pp. 2655-2662, Sep 2013

[45] I. Sadek, E. Seet, J. Biswas, B. Abdulrazak, and M. Mokhtari, "Nonintrusive vital signs monitoring for sleep apnea patients: A preliminary study," *IEEE Access,* vol. 6, pp. 2506-2514, 2018

[46] N. Lagakos, W. J. Trott, T. R. Hickman, J. H. Cole, and J. A. Bucaro, "Microbend fiber-optic sensor as extended hydrophone," *IEEE J. Quantum Electron.,* vol. 18, no. 10, pp. 1633-1638, 1982

[47] B. G. Grossman, T. Yongphiphatwong, and M. Sokol, "In situ device for salinity measurements (chloride detection) of ocean surface," *Opt. Laser Technol.,* vol. 37, no. 3, pp. 217-223, Apr 2005

[48] Stockholm, Sweden: COMSOL Multiphysics® v. 5.5. cn.comsol.com. COMSOL AB.

[49] G. A. Denu, Z. C. Liu, J. Fu, and H. X. Wang, "A finite element analysis of the effects of geometrical shape on the elastic properties of chemical vapor deposited diamond nanowire," *AIP Adv.,* vol. 7, no. 1, p. 015025, Jan 2017

[50] G. Sapra and P. Sharma, "Design and analysis of MEMS MWCNT/epoxy strain sensor using COMSOL," *Pramana,* vol. 89, no. 1, p. 10, 2017/06/20 2017

[51] M. D. Ainslie *et al.*, "Numerical modelling of mechanical stresses in bulk superconductor magnets with and without mechanical reinforcement," *Supercond. Sci. Technol.,* vol. 32, no. 3, p. 034002, Mar 2019

[52] Y. H. Lee, H. O. Kim, and Y. J. Kim, "Structural Characteristics of a Conical-Frustum-Patterned Stretchable Heater in an External-Force Environment," *J. Nanosci. Nanotechno.,* vol. 18, no. 9, pp. 6606-6610, Sep 2018

[53] A. V. Velamuri, K. Patel, I. Sharma, S. S. Gupta, S. Gaikwad, and P. K. Krishnamurthy, "Investigation of Planar and Helical Bend Losses in Single- and Few-Mode Optical Fibers," *J. Lightwave Technol.,* vol. 37, no. 14, pp. 3544-3556, 2019

[54] C. R. Hammond and S. R. Norman, "Silica based binary glass systems-refractive index behavior and composition in optical fibers," *Opt. Quantum Electron.,* vol. 9, no. 5, pp. 399-409, 1977

[55] P. Toupin, L. Brilland, D. Méchin, J. Adam, and J. Troles, "Optical Aging of Chalcogenide Microstructured Optical Fibers," *J. Lightwave Technol.,* vol. 32, no. 13, pp. 2428-2432, 2014

[56] G. Rault, J. L. Adam, F. Smektala, and J. Lucas, "Fluoride glass compositions for waveguide applications," *J. Fluorine Chem.,* vol. 110, no. 2, pp. 165-173, 2001/08/29/ 2001

[57] I. Byun and B. Kim, "Fabrication of three-dimensional PDMS microstructures by selective bonding and cohesive mechanical failure," *Microelectron. Eng.,* vol. 121, pp. 92-95, 2014/06/01/ 2014

[58] D. Donlagic and M. Zavrsnik, "Fiber-optic microbend sensor structure," *Opt. Lett.,* vol. 22, no. 11, pp. 837-839, Jun 1997

[59] N. Lagakos, J. H. Cole, and J. A. Bucaro, "Microbend fiber-optic sensor," *Appl. Optics,* vol. 26, no. 11, pp. 2171-2180, 1987/06/01 1987

[60] S. Q. Mawlud and N. Q. Muhamad, "Theoretical and Experimental Study of a Numerical Aperture for Multimode PCS Fiber Optics Using an Imaging Technique," *Chin. Phys. Lett.,* vol. 29, no. 11, p. 114217, 2012/11 2012

[61] W. J. Wadsworth *et al.*, "Very high numerical aperture fibers," *IEEE Photonics Technol. Lett.,* vol. 16, no. 3, pp. 843-845, 2004

[62] N. A. Issa, "High numerical aperture in multimode microstructured optical fibers," *Appl. Optics,* vol. 43, no. 33, pp. 6191-6197, 2004/11/20 2004

[63] B. Krishna, A. Chaturvedi, N. Mishra, and K. Das, "Nanomechanical characterization of SU8/ZnO nanocomposite films for applications in energy-harvesting microsystems," *J. Micromech. Microeng.,* vol. 28, no. 11, p. 115013, 2018/10/03 2018

[64] X. Wang, W. Gao, J. Hung, and W. Y. Tam, "Optical activities of large-area SU8 microspirals fabricated by multibeam holographic lithography," *Appl. Optics,* vol. 53, no. 11, pp. 2425-2430, 2014/04/10 2014

[65] H. M. Presby and D. Marcuse, "Refractive Index and Diameter Determinations of Step Index Optical Fibers and Preforms," *Appl. Optics,* vol. 13, no. 12, pp. 2882-2885, 1974/12/01 1974

[66] J. R. Dunklin, G. T. Forcherio, K. R. Berry, and D. K. Roper, "Gold Nanoparticle – Polydimethylsiloxane Thin Films Enhance Thermoplasmonic Dissipation by Internal Reflection," *J. Phys. Chem. C,* vol. 118, no. 14, pp. 7523-7531, 2014/04/10 2014

[67] J. Baumert and J. Hoffnagle, "Numerical method for the calculation of mode fields and propagation constants in optical waveguides," *J. Lightwave Technol.,* vol. 4, no. 11, pp. 1626-1630, 1986

[68] J.-P. Berenger, "A perfectly matched layer for the absorption of electromagnetic waves," *J. Comput. Phys.,* vol. 114, no. 2, pp. 185-200, 1994/10/01/ 1994

[69] D. Zhou, W. P. Huang, C. L. Xu, D. G. Fang, and B. Chen, "The perfectly matched layer boundary condition for scalar finite-difference time-domain method," *IEEE Photonics Technol. Lett.,* vol. 13, no. 5, pp. 454-456, 2001

[70] D. B. Davidson and M. M. Botha, "Evaluation of a Spherical PML for Vector FEM Applications," *IEEE Trans. Antennas Propag.,* vol. 55, no. 2, pp. 494-498, 2007

[71] S. Selleri, L. Vincetti, A. Cucinotta, and M. Zoboli, "Complex FEM modal solver of optical waveguides with PML boundary conditions," *Opt. Quantum Electron.,* vol. 33, no. 4, pp. 359-371, 2001/04/01 2001

[72] M. C. Hastings, B. Chiu, and D. W. Nippa, "Engineering the development of optical fiber sensors for adverse environments," *Nucl. Eng. Des.,* vol. 167, no. 3, pp. 239-249, 1997/04/01/ 1997

[73] C. Huang, W. Wang, W. Wu, and W. R. Ledoux, "Composite Optical Bend Loss Sensor for Pressure and Shear Measurement," *IEEE Sens. J.,* vol. 7, no. 11, pp. 1554-1565, 2007

[74] M. B. J. Diemeer and E. S. Trommel, "Fiber-optic microbend sensors: sensitivity as a function of distortion wavelength," *Opt. Lett.,* vol. 9, no. 6, pp. 260-262, 1984

[75] W. H. G. Horsthuis and J. H. J. Fluitman, "The development of fibre optic microbend sensors," *Sens. Actuators,* vol. 3, no. 2, pp. 99-110, 1983

[76] L. C. Wu, Q. Wang, M. J. Guo, C. Du, and Y. N. Zhang, "Characterization of displacement sensing based on fiber optic microbend losses," *Instrum. Sci. Technol.,* vol. 44, no. 5, pp. 471-482, 2016

[77] S. Jiguet, M. Judelewicz, S. Mischler, A. Bertch, and P. Renaud, "Effect of filler behavior on nanocomposite SU8 photoresist for moving micro-parts," *Microelectron. Eng.,* vol. 83, no. 4, pp. 1273-1276, 2006/04/01/ 2006

[78] L. R. Viannie, G. R. Jayanth, V. Radhakrishna, and K. Rajanna, "Fabrication and Nonlinear Thermomechanical Analysis of SU8 Thermal Actuator," *J. Microelectromech. Syst.,* vol. 25, no. 1, pp. 125-133, 2016

[79] Y. T. Tian, X. B. Shang, and M. J. Lancaster, "Fabrication of multilayered SU8 structure for terahertz waveguide with ultralow transmission loss," *J. Micro/Nanolith. MEMS MOEMS,* vol. 13, no. 1, p. 013002, Jan-Mar 2014

[80] M. Yang *et al.*, "A novel rare cell sorting microfluidic chip based on magnetic nanoparticle labels," *J. Micromech. Microeng.,* vol. 31, no. 3, p. 034003, 2021/02/08 2021

[81] V. Kumar and N. N. Sharma, "Synthesis of hydrophilic to superhydrophobic SU8 surfaces," *J. Appl. Polym. Sci.,* vol. 132, no. 18, p. 41934, 2015

[82] M. Baibarac, A. Radu, M. Cristea, R. Cercel, and I. Smaranda, "UV Light Effect on Cationic Photopolymerization of the SU8 Photoresist and Its Composites with Carbon Nanotubes: New Evidence Shown by Photoluminescence Studies," *J. Phys. Chem. C,* vol. 124, no. 13, pp. 7467-7476, 2020/04/02 2020

[83] M. Nordstroem, D. A. Zauner, A. Boisen, and J. Huebner, "Single-mode waveguides with SU-8 polymer core and cladding for MOEMS applications," *J. Lightwave Technol.,* vol. 25, no. 5, pp. 1284-1289, // 2007

[84] J. H. Shi and Z. P. Wang, "Designs of infrared nonpolarizing beam splitters with a Ag layer in a glass cube," *Appl. Optics,* vol. 47, no. 14, pp. 2619-2622, 2008/05/10 2008

[85] Y. B. Ovchinnikov, "A planar waveguide beam splitter," *Opt. Commun.,* vol. 220, no. 4, pp. 229-235, 2003/05/15/ 2003

[86] K. P. Sibin *et al.*, "Design and development of ITO/Ag/ITO spectral beam splitter coating for photovoltaic-thermoelectric hybrid systems," *Sol. Energy,* vol. 141, pp. 118-126, 2017/01/01/ 2017

[87] C. C. Homes, G. L. Carr, R. P. S. M. Lobo, J. D. LaVeigne, and D. B. Tanner, "Silicon beam splitter for far-infrared and terahertz spectroscopy," *Appl. Optics,* vol. 46, no. 32, pp. 7884-7888, 2007/11/10 2007

[88] L. Tao, S. Deng, H. Gao, H. Lv, X. Wen, and M. Li, "Experimental Investigation of the Dielectric Constants of Thin Noble Metallic Films Using a Surface Plasmon Resonance Sensor," *Sensors,* vol. 20, no. 5, p. 1505, 2020